Tribology in Industry

RESEARCH

Microstructural Evolution and Strain-Hardening Behavior in Hadfield Steel Railway Crossings

Gustavo Tressia[a],* , Tiago Tepedino[b] , Mohammad Masoumi[c] , Juan Ignacio Pereira[d]

[a]Instituto Tecnológico Vale, Ouro Preto, MG, Brazil,
[b]Loram do Brasil, Curitiba, PR, Brazil,
[c]Universidade Federal do ABC, Santo André, SP, Brazil,
[d]Escola de Engenharia de São Carlos, Universidade de São Paulo, São Paulo, SP, Brazil.
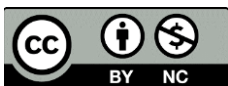
A B S T R A C T

This work examines defect (spalling) in a railway crossing (frog) removed from a heavy-haul railway after 120 Milling Gross Tons (MGT). The frog was manufactured using standard Hadfield steel. The steel microstructure evolution was analyzed to understand crack initiation and propagation during service. Scanning electron microscopy (SEM), X-ray diffraction, and electron backscattered diffraction (EBSD) methods were employed to characterize microstructural changes near the crack region. Furthermore, local mechanical properties were assessed using nanoindentation tests and sub size tensile tests. SEM analysis revealed that twinning is the primary work-hardening mechanism, with the absence of phase transformation confirmed by XRD. The interaction of dislocation walls and twin structures generated by twinning-induced plasticity increased the local hardness of Hadfield steel up to 8.5 GPa, substantially reducing ductility. Peak broadening of austenite phases was observed, indicating significant crystal defect densities under cyclic loading. Microstructural analysis in defect regions showed that these defects originated from the nucleation and propagation of cracks in grain boundaries with carbides. This investigation demonstrates that the reduced service life of the railway frog is associated with manufacturing process defects and contributes to understanding material deformation mechanisms, aiding in the development of more resilient steels for such applications.

1. INTRODUCTION

The growing demand for increased productivity, axle load, speed, and train size in railways has led to accelerated wear of components, higher operating costs, increased scrap generation, and pollutant emissions due to the need for replacement parts. The rapid wear of railway components can be linked to inadequate track conditions, improper material selection, and manufacturing defects. One of the main components of a railway is the turnout, whose useful life tends to be shorter than that of a rail, as it is a region of discontinuities subjected to high stress levels, with an association of wear and impact, among another factors [1].

On the railway turnout, the crossing is the region where the highest stress is concentrated. The contact stresses between the wheel and the rail in the crossing regions are up to four times higher than those promoted by the static load of the wheel [2]. Wear, rolling contact fatigue (RCF) and accumulated plastic deformation are the three damage mechanisms have been identified as the most detrimental to the life of a crossing nose [3]. Due to the high stresses imposed by the contacts and repeated impacts that the alligators are subjected to through the wheel passages, this component is commonly manufactured from austenitic manganese steel, or Hadfield steel. The Figure 1 shows the crossing and its main regions.
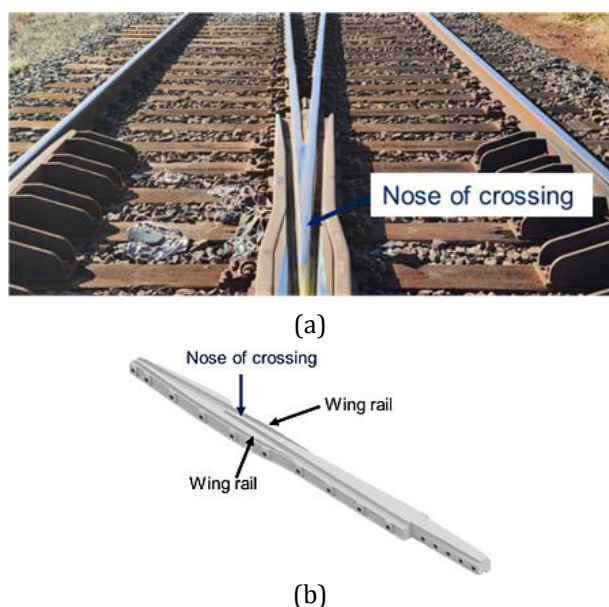

(a)

(b)

Fig 1. (a) crossing and (b) crossing regions.

Some works has focused on developing variations of austenitic manganese steel, aiming to increase the wear resistance and useful life of components, through changes in the chemical composition, to improve wear resistance and mechanical properties [4–7]. A successful study focused on obtaining Hadfield steels with microstructure with smaller austenitic grain size, aiming to increase toughness and hardness [8]. Austenitic manganese steels present low hardness (200 - 250 HV) before being subjected to service, with values lower than those of railway wheels. However, during severe conditions, involving high stress impact and wear, Hadfield steel show significant increases in hardness, exceeding 700 HV [9–15]. To overcome the low

initial hardness of Hadfield steels crossings to reduce de significant wear on initial phases of operation in the track, some railways adopt practices of prior hardening, subjecting these components to explosion hardening [16]. Other works focused on promoting an increase in the useful life of crossings through geometric design adjustments, aiming to reduce efforts due to contact and repeated impacts from the wheels [17–19].

However, regardless of the approach to be taken to increase the useful life of the railway crossing, it is important to initially know the behavior of Hadfield steel when subjected to use in the track. Therefore, this work will focus on characterizing the mechanical properties and microstructure at different depths of the nose of a crossing used on a heavy-haul railway. Techniques of Scanning Electron Microscopy (SEM), Electron Backscatter Diffraction (EBSD), Micro-tensile and nano-indentation methods are employed in this work.

2. EXPERIMENTAL PROCEDURE

A railway crossing (Figure 2) applied to a Heavy-Haul railway was analyzed after 120 MGT (Milling Gross Tons), not subjected to any prior hardening process (by explosion). The region of the crossing analyzed was the nose (Figure 2a), which had Spalling-type defects in severe condition (Figure 2c), making it possible to observe the density of cracks and defects using the liquid penetrant test (Figure 2b). The crossing was fabricated with Hadfield Steel with the chemical composition presented in Table 1, as specified by ASTM A-128 for grade B [20].

**Table 1**. Chemical composition of the crossing in wt. %.

(%)						
C	Mn	Cr	Mo	Si	P	S
1.20	13.70	0.10	0.22	0.64	0.041	0.006

The metallographic preparation of the samples was grinding and polishing up to 1 μm with water-based diamond suspensions, followed by an etching step with a 5% Nital solution (5 vol% nitric acid and 95 vol% alcohol) for 15s. An initial characterization was performed in the sample to identify the microstructural transformation regions via Scanning Electron Microscopy (SEM), using the JEOL JSM-6010LA

microscope. A detailed analysis using EBSD (Electron Backscattering Diffraction) was performed, using the FEI Quanta 650 FEG microscope, operating at 20 keV, step size of 0.25 μm in the 500x maps, 0.025 μm in the 5000x maps, and 0.007 μm in the 15000x map. For EBSD analysis, the samples were prepared using the similar metallographic preparation for SEM, with an additional step in a Minimet 1000 Buhler grinder-polisher machine with 0.04 μm colloidal silica for 2 hours.

(a)
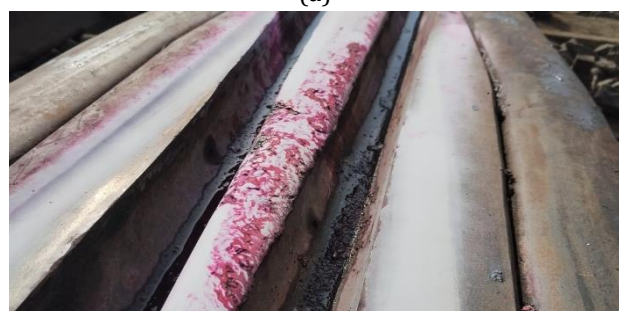
(b)

(c)

Fig. 2. (a) Identification of the spalling-type defect in a railway crossing, (b) nose of the crossing after liquid penetrant test and (c) Spalling-type defects in higher magnification.

X-ray diffraction was employed on un-etched samples, with an X-pert Pro Diffractometer with filtered CuKα radiation. A collection time of 2 s for each step was employed, in a continuous scan mode, and over the angular width 2θ= 35 to 65°, with angle step of 0.03°.

For the nano-hardness analysis, a Berkovich indenter at 1mN normal load was used. The micro-tensile test, with subsize specimens, were conducted in an Instron 3369 testing machine at a constant strain rate of 10-3 s-1 from the yield point to fracture. Bluehill® software was used to control the test parameters and data acquisition. Three test replicate was employed. The samples were manufactured by wire electrical discharge machining, with a thickness of 1 mm and a length of 10 mm (Figure 3c).
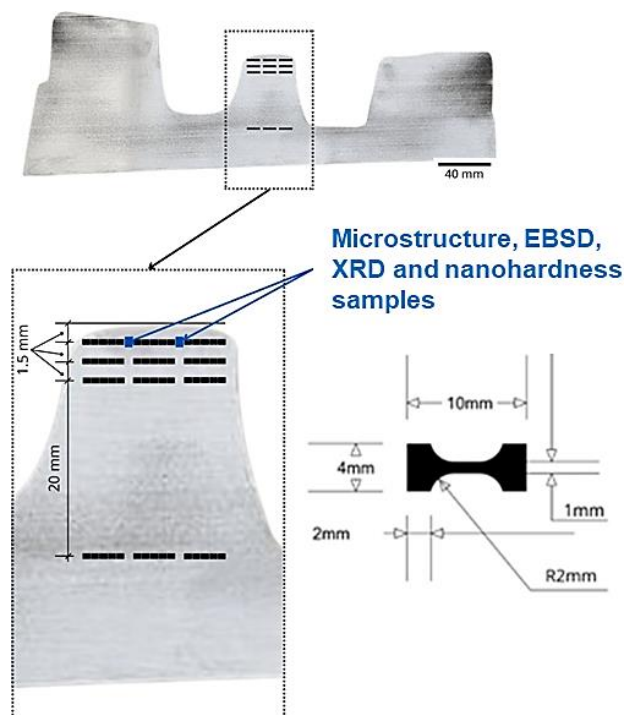

Fig. 3. Cross-section of the crossing analyzed, analysis and sample collection regions and subsize sample geometry.

Figure 3 shows sample collection regions of the railway crossing for microstructure, EBSD, XRD, nanohardness and tensile test analyses.

3. RESULTS

For the characterization of the microstructure beneath the surfaces, SEM analysis was conducted on the running band of the crossing (Fig. **4**). The surface on the top of the crossing exhibited spalling failure and surface cracks (see Fig. **4**c). A cross-sectional view of the microstructure revealed two distinct regions within the same sample, characterized by crack propagation parallel to both the surface and the base of the spalling (Fig. **4**d).
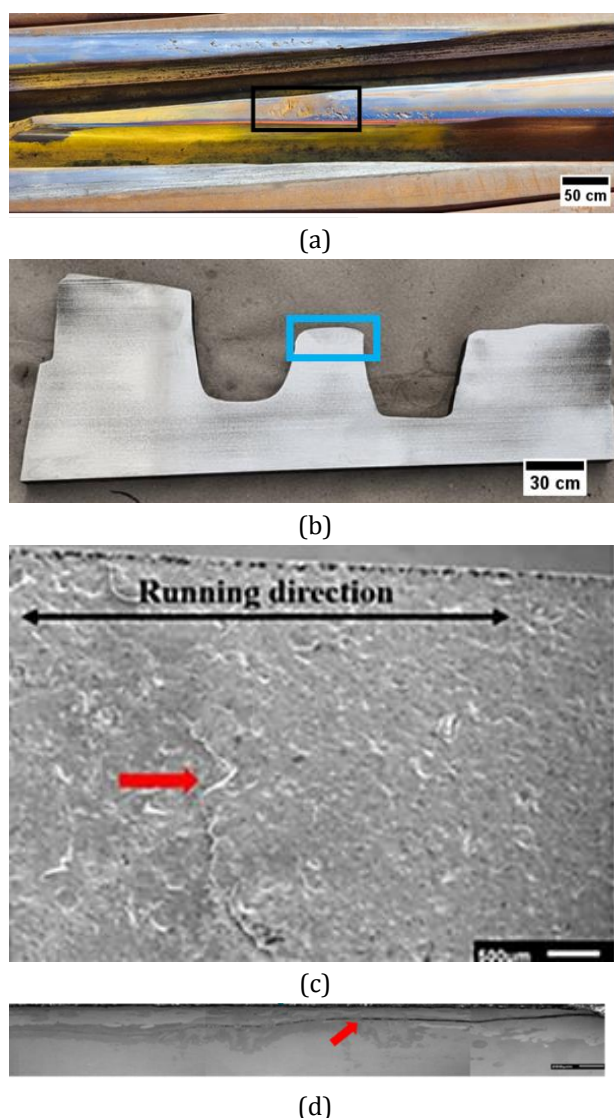
(a)

(b)

(c)

(d)

Fig. 4. Sample identification, (a) Hadfield crossing, (b) cross section of analyzed region, (c) worn surface on the top of the crossing (SE-SEM micrograph), (d) microstructure in the cross-section of the worn surface. The crack propagation is identified by the red arrows and the spalling area by the black box.

Figure 5 displays the cross-sectional microstructure of the area containing the crack analyzed via SEM. The red box highlights a specific region close to the crack, revealing a significant number of secondary cracks (black arrows) and the presence of continuous carbides along the grain boundaries (white arrows). In regions where carbides are present along the grain boundaries, some cracks can be observed, acting as stress concentrators, reducing fracture toughness and making these regions preferential sites for crack nucleation and propagation [21,22]. Additionally, from the cross-sectional analysis in Figure 5b, it is possible to notice areas with cracks at an early

stage and the presence of carbides, suggesting that cracks are nucleated in these carbide-rich regions. Precipitated carbides decrease impact and fracture toughness, and as a result, the component, in this case, the crossing, may not withstand the impacts and stresses imposed by the railway wheels. Carbides were observed in almost all regions analyzed. In the central regions, where heat dissipation is more difficult, higher fractions of carbides were observed.
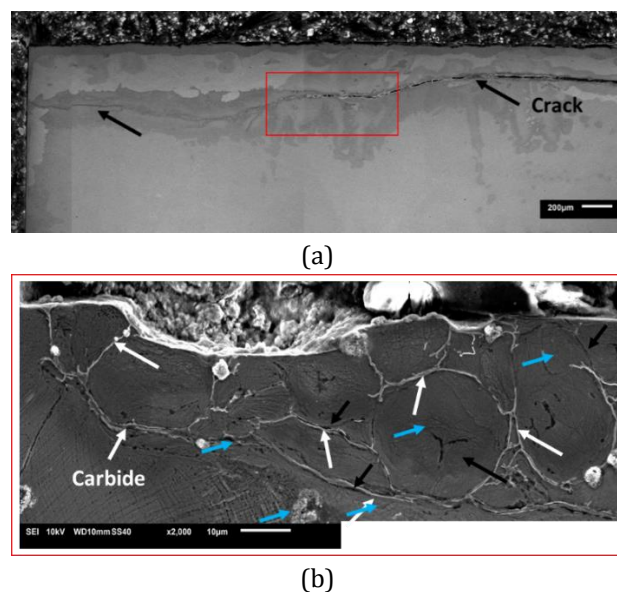

(a)

(b)

Fig. 5. SEM micrograph of the microstructure in cross section of the worn surface showing, a) a surface crack propagating in parallel direction throwing the microstructure, b) formation of twins in the region close to the crack. Formation of secondary cracks.

To enhance the metallurgical quality of crossings with carbide precipitates, several actions can be proposed: controlling the chemical composition and adopting an appropriate solubilization heat treatment. Reducing carbon content tends to decrease the propensity for carbide formation, while adding molybdenum extends the cooling time required, preventing carbide precipitation after solubilization treatment [22,23]. Solubilization heat treatments aim to dissolve phases, such as perlite and carbides, until the microstructure becomes entirely austenitic. To guarantee the complete dissolution of undesirable phases and prevent carbide formation, the temperature, heating time, and cooling rate must be adequately adjusted [23]. The formation of surface defects on this crossing is likely associated with the nucleation and propagation of cracks in carbide-rich regions, leading to the removal of large volumes of material.

Despite the cracks observed in Figure 5b, the Hadfield steel was able to absorb some of the energy and deformed, as evidenced by the twinning deformation mechanisms (blue arrows).

Figure 6 and Figure 7 present the cross-sectional microstructure of the spalling area. The presence of spalling can be associated to the surface cracks nucleation and the propagation through a work-hardened region close to the surface. The red box in Figure 6 highlights the microstructure, identifying the crack propagation in the region near the surface. The FEG-SEM micrograph (blue and black boxes) enables the identification of twins (blue arrows) as the primary deformation mechanism in the subsurface area. Figure 7 provides a detailed view of the twinning mechanism near the worn surface. The formation of a high density of deformation twins is evident. These twins are a key factor in strain-hardening, leading to the dynamic Hall-Petch effect, which results in ultrafine grain formation and increased hardness near the surface [24].
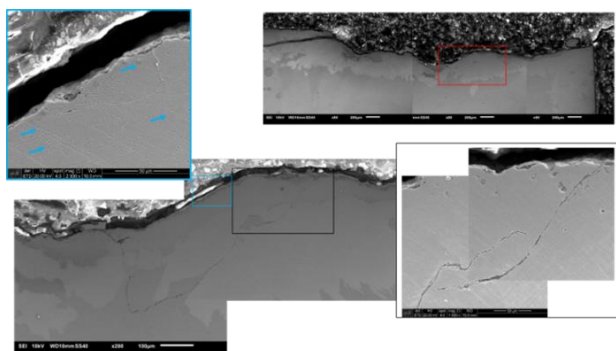

Fig. 6. Microstructure in the cross section of the worn surface with a surface crack. The red box shows the microstructure highly magnified, highlighting microstructure features like the crack junction (red arrow). The blue and black boxes show the formation of twins in the region close to the surface.
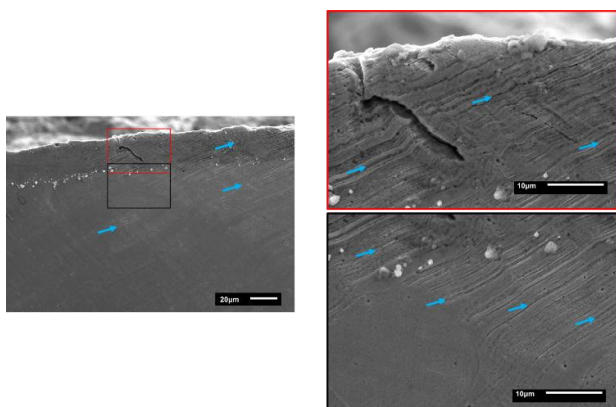

Fig. 7. Microstructure in the cross section showing the twin in the region close to the worn surface.

The figure illustrates that crack propagation is primarily transgranular, which is consistent with the literature [25] on deformation mechanisms in Hadfield steel under cyclic loading and impact conditions. The interaction between dislocations and deformation twins plays a crucial role in strain-hardening. Figures 5 to 7 demonstrate that the microstructural changes due to repeated stress and impact are characterized by crack nucleation at grain boundaries rich in carbides and the development of twinning structures. This suggest that the work-hardening mechanisms, particularly twinning, are responsible for increasing hardness near the surface, but they also contribute to crack formation and propagation.

To investigate phase transformations induced by deformation, XRD analyses were conducted in various regions of the crossing, both near the worn surface (Regions 2, 3, and 4 – deformed regions) and in the bulk of the crossing (Region 1 – undeformed region).

Figure 8 reveals that only austenite was identified. XRD patterns exhibit peaks of (111) and (200) planes corresponding to FCC austenite [9,26]. Although the micrographs displayed the presence of carbides in the grain boundary, XRD did not detect these phases due to their small quantity compared to austenite. Additionally, other phases, such as martensite induced by deformation in this type of steel, were not observed.
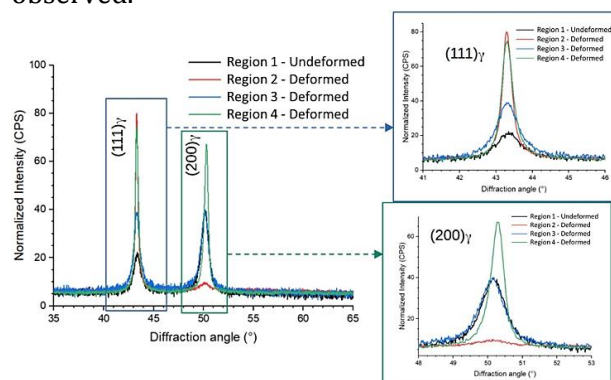

Fig. 8. XRD patterns in different regions of the crossing.

Hardness analysis in the subsurface, as function of the distance from the worn surface, reveals strain-induced hardening in the region close to the surface. The hardness profile indicates that hardening reaches a depth of approximately 8 mm. The maximum macro hardness found, of 350
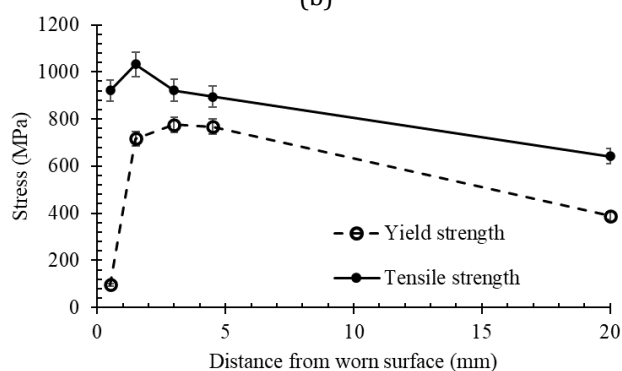
HB, was in the region closest to the surface, at approximately 1.5 mm. To understand in more detail the hardening of layers closest to the wear surface, nanohardness profile was carried out between 0.01 and 0.5 mm, from the surface.
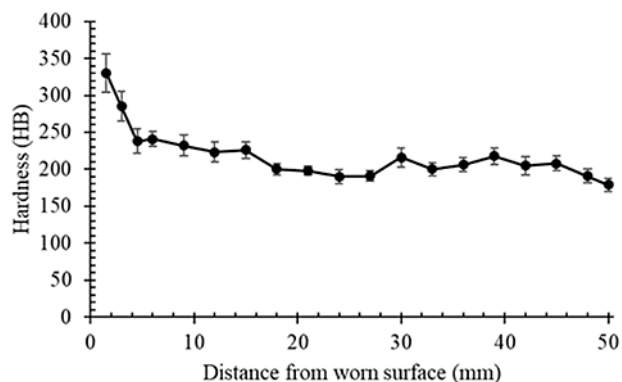
(a)
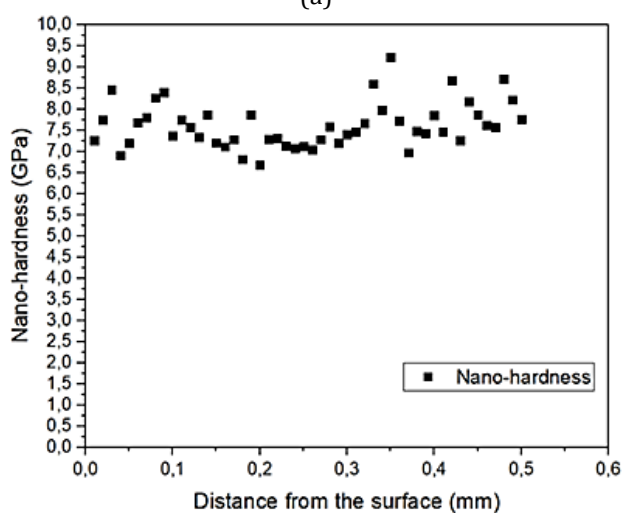
(b)

(c)

Fig. 9. (a) Hardness profile, (b) Nano-hardness profile and (c) tensile test results as function of the distance from the worn surface.

The results indicates that the nanohardness reaching an average value of 8 GPa up to 500 µm depth (see Figure 9b). Similar hardness was found in Hadfield steels subjected to wear in crushers [27], in railway crossing [10] and in laboratory sliding wear test [9]. The hardness of the material without deformation, located 50 mm from the worn surface, measured 200 HB. Comparing these hardness values, the deformed region exhibited a hardness 3.5 times higher. The tensile test results (Figure 9c) demonstrated that both yield and tensile strength limits are sensitive to the material's deformation level. In the region of higher deformation, that is, closer to the worn surface, yield strength and tensile strength were lower than in other regions of the material. It is suggested that, in this region, the material's deformation capacity had already been exhausted due to the demands imposed by the wheel and the presence of cracks, which drastically reduce the properties of the area. However, in intermediate regions between the worn and the core surface (without deformation), the values were higher. This outcome indicates that the material in these regions, with lower deformation intensities, still possesses the capacity to absorb energy and respond to the demands imposed by the passing of railway wheels.

The results of tensile tests (Figure 9c) are important to reinforce and justify preventive maintenance interventions on the crossings. The application of the preventive grinding process can be important, considering that the region closest to the surface has lower mechanical properties and that the adjacent layer has better mechanical properties compared to the surface and the core (material without deformation). Therefore, for railway practice, maintenance teams can limit the amount of material to be removed preventively, with the aim of removing part of the cracks and exposing a region of the material that has higher deformation capacity, and consequently greater resistance to wear.

Preventive rail grinding is a practice commonly applied on the world's main Heavy-Haul railways. This process guarantees the partial removal of RCF defects, as well as ensuring the correction of the rail profile, thus safeguarding a contact that allows for a better stress distribution. However, grinding of crossing is generally carried out in a corrective practice, often applied when the defect has already propagated and is at an advanced stage. The results found in this work show the importance of designing a grinding practice taking

precautions at crossings, in order to avoid large spreads of cracks and also remove a region of the material that not has the capacity to absorb the deformation imposed by the wheel contacts.

The EBSD analysis at the subsurface region, extending to 100 μm below the surface, provides significant insights into the accumulative plastic deformation occurring beneath the contact area. Figure 10 illustrates the initiation and propagation of cracks. These cracks initially nucleated at the contact interface between the train wheel and the rail surface due to the cumulative effects of fatigue impact and rolling contact stresses. As previously discussed, this region experiences extreme accumulative deformation, leading to a high concentration of defects, which accelerates the formation of microcracks. The band contrast image in Figure 10 highlights the formation of highly localized shear bands and FeMn twinning structures. However, it is important to note that FeMn twins could not be directly detected by EBSD, as the Kikuchi patterns and phase maps in this image solely reveal the presence of austenitic FCC-ɣ phases. The inability to detect FeMn twins through EBSD is attributed to the inherent limitations of the technique in identifying specific twinning within the FCC structure [28,29]. It is worth mentioning that the FCC crystal structure, which has the highest atomic packing factor (74%), is analogous to the HCP unit cell. Severe plastic deformation, as a result of extensive slippage, can alter the atomic packing configuration, leading to the formation of local defects. These defects, in turn, can result in HCP-type twinning, as observed in this figure.
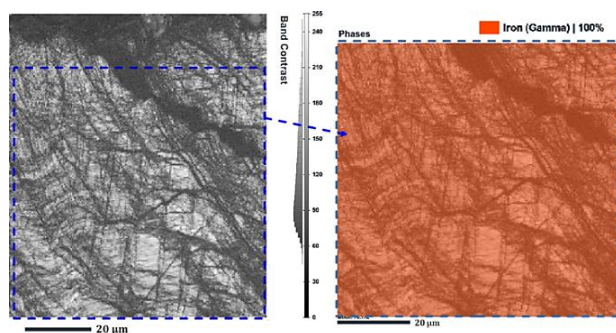

Fig. 10. Band contrast and phase maps at the subsurface region, illustrating the initiation and propagation of cracks beside the formation of highly localized shear bands and FeMn twinning structures.

Figure 11a presents the Z-direction Orientation Image Map (Z-OIM) of the longitudinal rail direction. In this map, cracks and twin interfaces are represented in black due to the absence of Kikuchi patterns, which inhibits their detection. Nevertheless, the color-coded map effectively illustrates the crystal and grain orientations. Visual inspection, along with statistical analysis using the Z-Inverse Pole Figure (Z-IPF) map, confirms the predominant crystal orientations of (102) to (101) within the FCC-ɣ matrix. It is well established that the <101> direction is the most densely packed atomic orientation, primarily facilitating atomic plane sliding during plastic deformation, which accounts for the observed twinning. The image suggests that crack propagation occurs along the (101) grain boundary, likely driven by the high Schmid factor associated with this orientation.

Figure 11b displays the Kernel Average Misorientation (KAM) map, which quantifies grain internal distortion by calculating the misorientation of the five nearest pixels relative to a reference point, with a threshold of 5° to minimize the influence of grain and subgrain boundaries [30]. The regions exhibiting high KAM values, indicated in red, clearly demonstrate significant internal energy within the material. Figure 11c illustrates the crystallographic defect densities as determined by the Entrywise Norm of the Nye Tensor. This analysis reveals that the average dislocation density is approximately 7.6×10^{14} m-2, with a peak density reaching around 1.8×10^{15} m-2, which is exceptionally high for Hadfield steel [10,21]. These findings suggest that while the material performs well under operating conditions, adjustments during maintenance periods may be necessary to manage the high defect densities effectively. During the deformation process of Hadfield steel, de work hardening and strength of the material increasing, but the fracture strain decreased and resulting in ductility loss, promoting the occurrence of microfractures [31], which evolve into spalling-type defects shown in the Figure 2c. As shown in the tensile tests (Figure 9b), dislocation density measurements also suggest that regions closer to the surface need to be removed by preventive procedure, exposing regions with a greater capacity to absorb the stresses imposed by wheel contact.
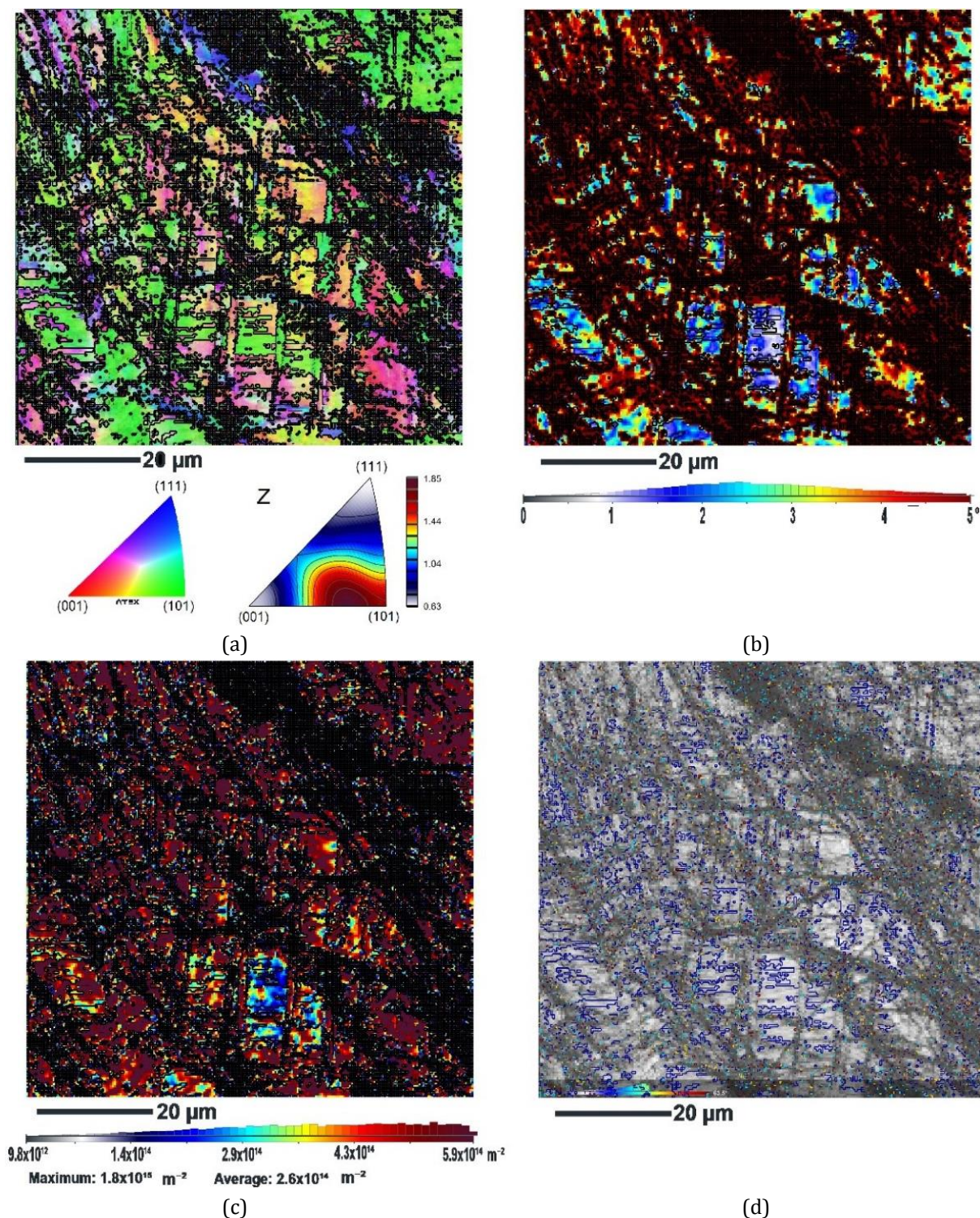
Fig. 11. (a) Z-OIM, (b) KAM, (c) crystallographic defect densities, and (d) Σ3n special boundaries maps obtained from EBSD data.

Twins in FCC materials like austenitic steel form special boundaries described by Coincidence Site Lattice (CSL) theory, where boundaries are characterized by Σ - values. These values represent the degree of lattice coincidence, with lower Σ values indicating more ordered and lower-energy boundaries. The orientation between grains can be described by Axis/Angle pairs, such as Σ3 twins, which represent a 60° rotation around the <111> axis, or Σ9 with a 38.94° rotation around <110>. Euler angles are another way to describe grain orientations, often used in EBSD analysis. Figure 11d shows that 10.2% of the total boundary length (28,900 μm)

in the EBSD map consists of twin-related special boundaries. Among these, 7.21% correspond to Σ3 (60° around <111>), 1.31% to Σ9 (38.94° around <110>), 0.58% to Σ27a (31.59° around <110>), and 1.12% to Σ27b (35.43° around <210>), demonstrating the prevalence of Σ3 twins under plastic deformation.
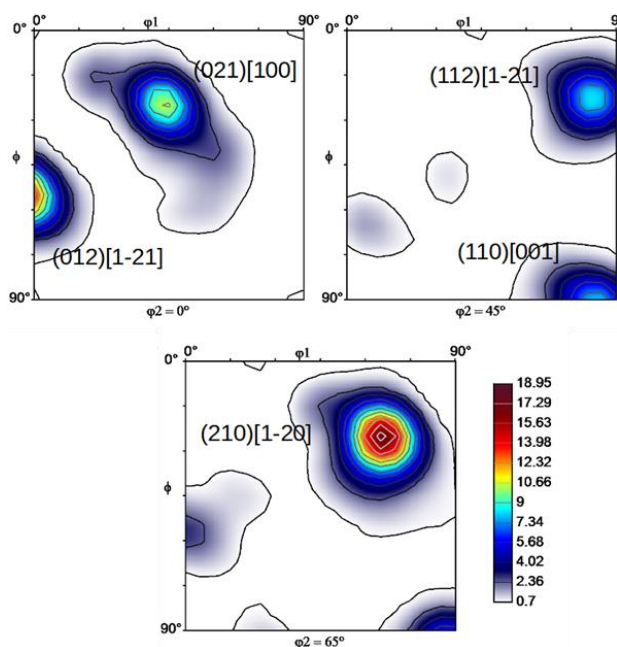

Fig. 12. ODFs at constant $\varphi2=0°$, 45°, and 65° to present the most known crystallographic textures

ODF from individual orientations was done by kernel density estimation using Fourier series on the orientation space that associates to each orientation volume percentage of crystals in the obtained EBSD data. Figure 12 shows ODFs at constant $\varphi2=0°$, 45°, and 65° to present the most known crystallographic textures in FCC structure materials [32]. The (210) [1-20] and (012) [1-21] crystallographic textures were estimated with the highest volumetric fraction at the predominant texture in this region, where the (210) atomic plane is parallel to the rolling direction, while [1-20] and [1-21] were estimated as atomic directions parallel to the rolling direction. The significant presence of these orientations suggests a strong correlation with the twinning phenomenon, as these specific crystallographic textures align closely with the conditions that favor twinning in FCC structures. The [1-20] and [1-21] directions are likely to be involved in the activation of twinning on the {111} planes due to their alignment with the twinning shear direction, leading to the formation of twin boundaries.

This alignment not only facilitates atomic plane slippage but also promotes the nucleation and growth of twins, thereby contributing to the observed texture and the mechanical behavior of the material under rolling conditions [33]. The high Schmid factors associated with these orientations further justify their role in enhancing twinning activity, ultimately influencing the overall deformation mechanisms in the FCC matrix.

Figure 13a presents the variation in the frequency of misorientation changes between neighboring points, which serves as an effective method for classifying sub-grain and grain boundaries. In this analysis, low-angle boundaries (LABs) with misorientations less than 5° account for approximately 25% of the volume, while medium-angle boundaries with misorientations between 5° and 15° comprise about 15% of the volume. As the misorientation increases, the internal energy also rises, reaching a critical threshold at 15°, which defines high-angle boundaries (HABs). These HABs, constituting about 60% of all boundaries, are known to act as significant barriers to dislocation movement due to their high internal energy. Notably, within these HABs, approximately 10.2% are classified as Coincidence Site Lattice (CSL) boundaries, specifically Σ3n twin boundaries [3,4]. Interestingly, these twinning boundaries, despite their higher misorientation angles (greater than 15°), exhibit lower internal energy, akin to that of low-angle boundaries, which is a unique characteristic of FeMn austenitic steel.

In addition, Figure 13b illustrates the distribution of Kernel Average Misorientation (KAM) values, showing that about 50% of the total KAM values correspond to low KAM (<0.5°), indicating regions with less internal energy. Conversely, 40% of the grains are classified as highly deformed ("hard") grains, characterized by significant local distortion. Furthermore, Figure 13c depicts the overall crystallographic defect densities, revealing an average dislocation density of approximately 7.6×10^{14} m-2, with peak densities reaching around 1.8×10^{15} m-2, which is exceptionally high for Hadfield steel. These findings underscore the substantial defect densities and internal stresses present in the material, which have critical implications for its mechanical performance and durability.
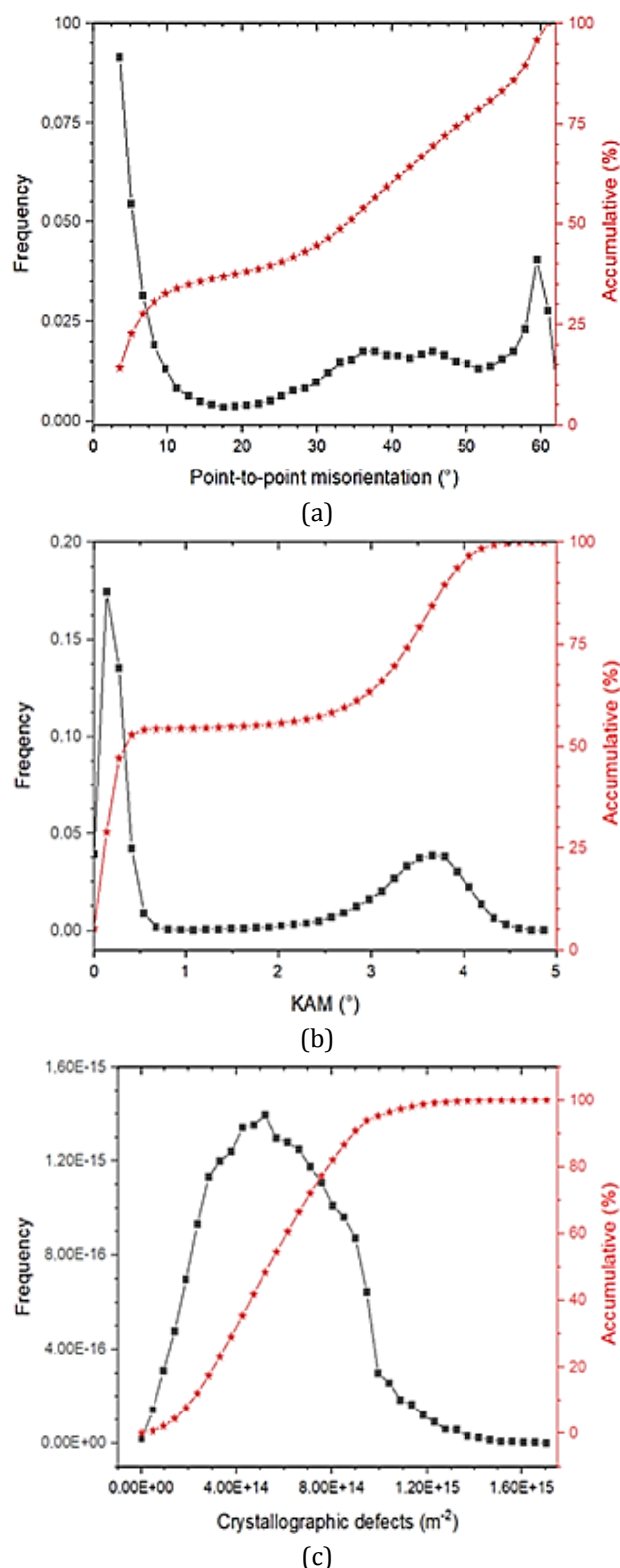
(a)

(b)

(c)

Fig. 13. (a) Variation in the frequency of misorientation changes between neighboring points, (b) distribution of KAM values, and (c) crystallographic defect densities variation.

The study of the Hadfield steel railway crossing, which had undergone 120 million gross tons (MGT) of service, revealed that twinning was the primary mechanism leading to significant strain-

induced hardening and increased hardness up to 8 GPa, although this also reduced ductility. SEM analysis showed the presence of cracks and spalling on the crossing surface, with carbides at grain boundaries acting as stress concentrators, and XRD confirmed the presence of austenite without significant phase transformation. The EBSD analysis further clarifies these findings by highlighting the inability of the technique to detect FeMn twins directly, due to limitations in identifying specific twinning within the FCC structure. The alignment of the [1-20] and [1-21] directions with the twinning shear direction on the {111} planes support the observed crystallographic textures and the role of twinning in the material's deformation behavior. The study also identified high dislocation densities, reaching up to 1.8×10^{15} m-2, which are exceptionally high for Hadfield steel and likely contribute to the material's performance under operating conditions. The presence of HABs, which constitute about 60% of all boundaries and act as barriers to dislocation movement, further explains the strain-hardening effects observed. Interestingly, within these HABs, approximately 10.2% were classified as $\Sigma 3n$ twin boundaries, which, despite their higher misorientation angles, exhibited lower internal energy similar to low-angle boundaries, a unique characteristic of FeMn austenitic steel. These combined results suggest that while the material exhibits robust performance, the high defect densities and complex twinning behaviors necessitate careful management during maintenance to optimize durability and service life.

4. CONCLUSIONS

Upon analyzing the worn surface of the Hadfield steel crossing, spalling failure was observed at the top of the surface. A detailed examination of the microstructure in the region near the failure allowed for the following conclusions:

- The material exhibited the presence of carbides in grain boundaries, which acted as sites for crack nucleation and propagation. Observing cracks initiating in regions with carbides suggests that the defects found on the crossing surface are related to the presence of carbides.

- Regular railway operation induced strain-hardening, increasing the hardness up to 8 GPa. Surface crack nucleation occurred in these regions, resulting in subsurface cracking.

- A very high deformation induced hardness was controlled by the density of the deformation induced twins and dislocation boundaries.

- The EBSD map confirms that mechanical twinning is the dominant plastic deformation mechanism near the surface, as evidenced by the high misorientation in areas where twins are present.

- The results of tensile tests as a function of the distance from the worn surface, show that the closer the surface, the lower the material's capacity to absorb the imposed stress, which leads to the nucleation and propagation of cracks. Therefore, it is highly recommended to adopt preventive practices, such as grinding, to remove a deformed layer with defects, restoring the material's capacity to absorb the deformation and taking longer for the generation of defects.

Acknowledgement

REFERENCES

[1] S. L. Guo, D. Y. Sun, F. C. Zhang, X. Y. Feng, and L. H. Qian, "Damage of a Hadfield steel crossing due to wheel rolling impact passages," *Wear*, vol. 305, no. 1–2, pp. 267–273, Jan. 2013, doi: 10.1016/j.wear.2013.01.019.

[2] M. Wiest, W. Daves, F. D. Fischer, and H. Ossberger, "Deformation and damage of a crossing nose due to wheel passages," *Wear*, vol. 265, no. 9–10, pp. 1431–1438, May 2008, doi: 10.1016/j.wear.2008.01.033.

[3] R. Skrypnyk, U. Ossberger, B. A. Pålsson, M. Ekh, and J. C. O. Nielsen, "Long-term rail profile damage in a railway crossing: Field measurements and numerical simulations," *Wear*, vol. 472–473, p. 203331, Jun. 2020, doi: 10.1016/j.wear.2020.203331.

[4] E. R. Magdaluyo, M. S. Ausa, R. J. Tinio, "Gouging Abrasion Resistance of Austenitic Manganese Steel with Varying Titanium," *Proceedings of the World Congress on Engineering,* vol. 2, pp. 1-4, Jul. 2015.

[5] Z.-M. He, Q.-C. Jiang, S.-B. Fu, and J.-P. Xie, "Improved work-hardening ability and wear resistance of austenitic manganese steel under non-severe impact-loading conditions," *Wear*, vol. 120, no. 3, pp. 305–319, Dec. 1987, doi: 10.1016/0043-1648(87)90024-x.

[6] D. Canadinc, H. Sehitoglu, I. Karaman, Y. I. Chumlyakov, and H. J. Maier, "The role of nitrogen on the deformation response of hadfield steel single crystals," *Metallurgical and Materials Transactions A*, vol. 34, no. 9, pp. 1821–1831, Sep. 2003, doi: 10.1007/s11661-003-0148-3.

[7] E. G. Moghaddam, N. Varahram, and P. Davami, "On the comparison of microstructural characteristics and mechanical properties of high-vanadium austenitic manganese steels with the Hadfield steel," *Materials Science and Engineering A*, vol. 532, pp. 260–266, Oct. 2011, doi: 10.1016/j.msea.2011.10.089.

[8] B. N. Venturelli, E. Albertin, and C. R. De Farias Azevedo, "The effect of the austenite grain refinement on the tensile and impact properties of cast Hadfield steel," *Materials Research*, vol. 21, no. 5, Aug. 2018, doi: 10.1590/1980-5373-mr-2018-0069.

[9] G. Tressia and A. Sinatora, "Effect of the normal load on the sliding wear behavior of Hadfield steels," *Wear*, vol. 520–521, p. 204657, Feb. 2023, doi: 10.1016/j.wear.2023.204657.

[10] O. A. Zambrano, G. Tressia, and R. M. Souza, "Failure analysis of a crossing rail made of Hadfield steel after severe plastic deformation induced by wheel-rail interaction," *Engineering Failure Analysis*, vol. 115, p. 104621, May 2020, doi: 10.1016/j.engfailanal.2020.104621.

[11] P. H. Adler, G. B. Olson, and W. S. Owen, "Strain hardening of Hadfield manganese steel," *Metallurgical Transactions A*, vol. 17, no. 10, pp. 1725–1737, O1-4ct. 1986, doi: 10.1007/bf02817271.

[12] X. Y. Feng, F. C. Zhang, Z. N. Yang, and M. Zhang, "Wear behaviour of nanocrystallised Hadfield steel," *Wear*, vol. 305, no. 1–2, pp. 299–304, Nov. 2012, doi: 10.1016/j.wear.2012.11.038.

[13] M. A. Shtremel, I. A. Kovalenko, "On the work hardening mechanism of Hadfield steel," *Physics of Metals and Metallography*, vol. 63, pp. 158–166, 1987.

[14] Y. N. Dastur and W. C. Leslie, "Mechanism of work hardening in Hadfield manganese steel," *Metallurgical Transactions A*, vol. 12, no. 5, pp. 749–759, May 1981, doi: 10.1007/bf02648339.

[15] Y. N. Dastur and W. C. Leslie, "The mechanism of rapid work hardening in Hadfield manganese steel," *in Elsevier eBooks*, 1979, pp. 619–623. doi: 10.1016/b978-1-4832-8412-5.50106-5.

[16] F. C. Liu, B. Lv, F. C. Zhang, and S. Yang, "Enhanced work hardening in Hadfield steel during explosive treatment," *Materials Letters*, vol. 65, no. 15–16, pp. 2333–2336, May 2011, doi: 10.1016/j.matlet.2011.05.041.

[17] B. A. Pålsson, "Optimisation of railway crossing geometry considering a representative set of wheel profiles," *Vehicle System Dynamics*, vol. 53, no. 2, pp. 274–301, Jan. 2015, doi: 10.1080/00423114.2014.998242.

[18] V. L. Markine and C. Wan, "Performance Optimised Geometry of Railway crossings: Design and implementation," *International Journal of Railway Technology*, vol. 5, no. 2, pp. 1–25, Jan. 2016, doi: 10.4203/ijrt.5.2.1.

[19] C. Wan, V. Markine, and R. Dollevoet, "Robust optimisation of railway crossing geometry," *Vehicle System Dynamics*, vol. 54, no. 5, pp. 617–637, Feb. 2016, doi: 10.1080/00423114.2016.1150495.

[20] *Standard Specification For Steel Castings, Austenitic Manganese*, ASTM-A128, 2012.

[21] L. B. Varela, G. Tressia, M. Masoumi, E. M. Bortoleto, C. Regattieri, and A. Sinatora, "Roller crushers in iron mining, how does the degradation of Hadfield steel components occur?," *Engineering Failure Analysis*, vol. 122, p. 105295, Feb. 2021, doi: 10.1016/j.engfailanal.2021.105295.

[22] M. Lindroos et al., "The deformation, strain hardening, and wear behavior of Chromium-Alloyed Hadfield steel in abrasive and impact conditions," *Tribology Letters*, vol. 57, no. 3, Jan. 2015, doi: 10.1007/s11249-015-0477-6.

[23] J. O. Olawale, S. A. Ibitoye, and M. D. Shittu, "Workhardening behaviour and microstructural analysis of failed austenitic manganese steel crusher jaws," *Materials Research*, vol. 16, no. 6, pp. 1274–1281, Aug. 2013, doi: 10.1590/s1516-14392013005000144.

[24] P. C. Machado, J. I. Pereira, J. J. Penagos, T. Yonamine, and A. Sinatora, "The effect of in-service work hardening and crystallographic orientation on the micro-scratch wear of Hadfield steel," *Wear*, vol. 376–377, pp. 1064–1073, Apr. 2017, doi: 10.1016/j.wear.2016.12.057.

[25] S. Dhar, H. K. Danielsen, S. Fæster, C. Rasmussen, Y. Zhang, and D. J. Jensen, "Crack formation within a Hadfield manganese steel crossing nose," *Wear*, vol. 438–439, p. 203049, Sep. 2019, doi: 10.1016/j.wear.2019.203049.

[26] R. Xiong, H. Peng, H. Si, W. Zhang, and Y. Wen, "Thermodynamic calculation of stacking fault energy of the Fe–Mn–Si–C high manganese steels," *Materials Science and Engineering A*, vol. 598, pp. 376–386, Jan. 2014, doi: 10.1016/j.msea.2014.01.046.

[27] P. C. Machado, J. I. Pereira, and A. Sinatora, "Subsurface microstructural dynamic recrystallization in multiscale abrasive wear," *Wear*, vol. 486–487, p. 204111, Sep. 2021, doi: 10.1016/j.wear.2021.204111.

[28] A. Behravan, A. Zarei-Hanzaki, S. M. Fatemi, H. F. G. De Abreu, and M. Masoumi, "The effect of aging temperature on microstructure and tensile properties of a novel designed FE–12MN–3NI Maraging-TRIP steel," *Steel Research International*, vol. 90, no. 2, Aug. 2018, doi: 10.1002/srin.201800282.

[29] M. N. Da Silva Lima et al., "Influence of cold deformation on microstructure, crystallographic orientation and tensile properties of an experimental austenitic Fe–26Mn-0.4C steel," *Journal of Materials Research and Technology*, vol. 19, pp. 7–19, May 2022, doi: 10.1016/j.jmrt.2022.05.020.

[30] S.-S. Rui et al., "EBSD analysis of cyclic load effect on final misorientation distribution of post-mortem low alloy steel: A new method for fatigue crack tip driving force prediction," *International Journal of Fatigue*, vol. 113, pp. 264–276, Apr. 2018, doi: 10.1016/j.ijfatigue.2018.04.016.

[31] W.-S. Lee, T.-H. Chen, "Plastic deformation and fracture characteristics of Hadfield steel subjected to high-velocity impact loading," *J Mechanical Engineering Science*, vol. 216, pp. 971-982, Mar. 2016.

[32] M. N.S. Lima, W. M. Ferreira, C. D. Andrade, H. F. G. Abreu, J. Klug, M. Masoumi, "Microstructure and Texture Evolution of Different High Manganese Cast Steels During Hot Deformation and Subsequent Treatment," in: CBECiMat - Brazilian Congress of Materials Science and Engineering, Feb. 2016.

[33] H. Idrissi, K. Renard, L. Ryelandt, D. Schryvers, and P. J. Jacques, "On the mechanism of twin formation in Fe–Mn–C TWIP steels," *Acta Materialia*, vol. 58, no. 7, pp. 2464–2476, Jan. 2010, doi: 10.1016/j.actamat.2009.12.032.